EJTP **11, No. 30** (2014) 9–26 *Electronic Journal of Theoretical Physics*

Majorana Returns: the Dirac-Boltzmann Connection

S. Succi*[1,2], S. Palpacelli[3], M. Mendoza[4] and H.J. Herrmann[4]

[1] *Istituto Applicazioni Calcolo, CNR, via dei Taurini 19, 00185, Roma, Italy*
[2] *Physics Department, Harvard University, Cambridge MA, 02138, USA,*
[3] *Numidia srl, via G. Peroni, 130, 00131, Roma, Italy,*
[4] *ETH, Inst. Bldg Mat, HIF, CH-8093, Zuerich, Switzerland*

Received 30 October 2013, Accepted 16 December 2013, Published 15 January 2014

Abstract: Formal and substantial analogies between the Boltzmann equation of classical statistical physics and the Dirac equation for relativistic quantum mechanics are discussed, with special emphasis on the Majorana representation of the Dirac equation, in which all matrices are real. It is shown that this property is instrumental in turning the Boltzmann-Dirac analogy into an efficient computational method for quantum problems, the so-called quantum lattice Boltzmann (QLB) method. Selected applications of the QLB method to Anderson localization in Bose-Einstein condensates and electron transport in graphene are presented and commented on. Finally, future prospects of QLB applications for quantum computing and the simulation of quantum field theories, are briefly mentioned.

Keywords: Boltzmann Equation; Dirac Equation; Majorana representation; Quantum Statistical Physics; Boltzmann-Dirac Analogy; Quantum Lattice Boltzmann; Quantum Computing
PACS (2010): 05.30.-d; 05.20.-y; 05.20.Dd; 04.50.-h; 03.65.Pm; 03.70.+k

1. Boltzmann and Dirac

Ludwig Boltzmann and Paul Dirac stand out as towering figures in modern science, the equations bearing their names serving as corner stones of two paramount areas of theoretical physics, statistical mechanics and relativistic quantum field theory, respectively. Although these disciplines deal with different problems in general, they exhibit several points of contact, primarily because of the inherently statistical character of relativistic quantum field theory. These commonalities are reflected by a mathematical analogy between the Boltzmann and Dirac equations, as we shall detail in the sequel. This is at first sight surprising, since the Dirac equation describes the space-time evolution of

* Email:succi@iac.cnr.it, saurosucci@harvard.edu

complex-valued spinorial wavefunction, whereas the Boltzmann equation deals with the evolution of a scalar density in six-dimensional phase-space. Notwithstanding this major structural difference, it should be noted that both equations are based on a hyperbolic, two-step Stream-Collide dynamics, which prepares the ground for the aforementioned analogy and sets the stage for Majorana's contribution. It is indeed well (or maybe not so well) known, that among the very many possible representations of the Dirac equation, there is one, due to Majorana, in which all matrices are *real* [1]. The resulting notion of Majorana fermions, i.e. spin 1/2 particles which coincide with their antiparticles, is gaining considerable interest in modern theoretical physics, as beautifully discussed in a recent essay by Wilczek [2]. Here, we wish to put forward yet another angle of interest of the Majorana representation, namely the fact that it permits to turn the Boltzmann-Dirac analogy into a concrete computational tool for the simulation of quantum wave equations, namely the quantum lattice Boltzmann (QLB) method [3].

2. Boltzmann to Navier-Stokes versus Dirac to Schroedinger

As noted above, both Boltzmann and Dirac equations are based on a first-order, hyperbolic, Stream-Collide dynamics, in which space and time come on the same footing. This stands in stark contrast with the two major equations which stem from Boltzmann's and Dirac's equations, namely the Navier-Stokes equation of fluid mechanics and the Schroedinger equation of non-relativistic quantum mechanics, which both involve first-order time derivatives and second order spatial ones. This is no coincidence, the broken balance between space and time being due, in both cases, to the elimination of "fast" degrees of freedom, which are irrelevant to the reduced description, namely hydrodynamics versus kinetic theory and non-relativistic versus relativistic quantum mechanics. This broken balance leads to deep and far-reaching consequences on the mathematical structure of the equations; in particular it prompts the emergent Advection-Diffusion paradigm out of the microscopic Stream-Collide dynamics.

To set the framework, let us write down the two equations in full display. The Boltmann equation reads as follows:

$$\partial_t f + v^a \nabla_a f = C(f, f) \tag{1}$$

where $f = f(x, v; t)$ is the probability density of finding a particle around position x at time t with velocity v, and $C(f, f)$ describes the change in f due to short-range collisions with other particles. The latin index $a = x, y, z$ runs over spatial dimensions and Einstein summation rule is assumed. The left hand side represents the particle free-streaming (in the absence of external forces, for simplicity), while the right-hand side is the collisional step steering the distribution function to a local Maxwell equilibrium f^{eq}.

The Dirac equation, in Majorana form, reads as follows

$$\partial_t \psi_i + S^a_{ij} \nabla_a \psi_j = M_{ij} \psi_j \tag{2}$$

where S^a_{ij} are the three Majorana streaming matrices and M_{ij} is the mass matrix, acting upon the complex 4-spinor ψ_i, $i = 1, 4$. Here again, the lhs describes the free streaming

of the spinors, while the rhs can be regarded as a simple form of local collision between the four spinorial components. Note, in fact, that in physical units, the mass matrix is a frequency, prefactored by the Compton frequency $\omega_c = mc^2/\hbar$.

2.1 Elimination of fast modes

In the classical (Boltzmann to Navier-Stokes) case, the fast degrees of freedom are non-equilibrium excitations on top of Maxwell-Boltzmann local equilibria. The strength of nonequilibrium excitations versus local equilibrium, scales approximately like the Knudsen number $Kn = \frac{l_\mu}{l_M}$, where l_μ is the molecular mean free path and l_M is the smallest hydrodynamic scale (in a turbulent flow this would be the Kolmogorov length). The Knudsen number serves as a smallness parameter, to derive Navier-Stokes hydrodynamics as a weak non-equilibrium expansion of the Boltzmann equation. Formally, one expands both the Boltzmann distribution and space-time derivatives in the Knudsen number as follows:

$$f = f^0 + Knf^1 + \dots \tag{3}$$

$$\partial_x = Kn\partial_{x_1} + \dots \tag{4}$$

$$\partial_t = Kn\partial_{t_1} + Kn^2\partial_{t_2} + \dots \tag{5}$$

where f^0 is the local Maxwell equilibrium, and x_1, t_1 and t_2 are multiscale space and time, respectively. Lengthy but elementary algebra (Chapman-Enskog asymptotic expansion) shows that at zeroth order, $f = f^0$, one recovers the Euler equations of inviscid hydrodynamics, whereas at first order, the dissipative Navier-Stokes equations are obtained. Higher order truncations, known as Burnett or super-Burnett, have met with limited success, since they are exposed to basic instabilities, a signal of the fact that the Chapman-Enskog expansion is only asymptotically convergent. The take-home message is that, by expanding and truncating, some of the original information contained in the Boltzmann equation gets lost in the process, and this is the reason why the Navier-Stokes equation acquire a Laplacian-driven dissipative term $\nu\Delta\vec{u}$, ν being the fluid kinematic viscosity and $\vec{u}$ the fluid flow. This stands in stark contrast with the Boltzmann representation, in which dissipation, hence irreversibility, does not stem from any diffusion process (the Laplacian), but is inherently built within the collision operator, which drives the distribution function f towards its local equilibrium f^{eq}, according to the celebrated Boltzmann's H-theorem. Note that such process is completely local in space, consistently with the point-like character of the Boltzmann molecules. A similar procedure applies to the transition from the Dirac to Schroedinger equation, the smallness parameter being now the ratio of particle to light speed, $\beta = v/c$, or, equivalently, the ratio of the De-Broglie to Compton wavelength, $\beta = \lambda_B/\lambda_C$, where $\lambda_B = \hbar/mv$ and $\lambda_C = \hbar/mc$. Here, the trick is to express the spinor in the form of a symmetric and antisymmetric combination:

$$\phi_\pm = \frac{1}{\sqrt{2}}(\psi_1 \pm i\psi_2)e^{-i\omega_c t} \tag{6}$$

For simplicity, we have considered a spin 1/2 fermion in $d = 1$, so that ψ_1 and ψ_2 are the chiral components moving along the $\mp$ directions along the given axis, say z. In the absence of magnetic fields, the two components are indistinguishable, so that only one needs to be retained and the four-spinor collapses to a bi-spinor. It is an easy matter to show that, under the Dirac dynamics, the antisymmetric component oscillates at a frequency $2\omega_c$ and with an amplitude $O(\beta^2)$ with respect to the symmetric mode. More, precisely the fast-mode elimination proceeds through the assumption

$$|\partial_t \phi_-| << 2\omega_c |\phi_-| \tag{7}$$

which is the usual non-relativistic limit $E << 2mc^2$, in wave-like language. As a result, in the non-relativistic limit, $\beta \to 0$, the antisymmetric mode decouples from the dynamics, and the Dirac equation reduces to the non-relativistic Schroedinger equation. It is this elimination of the fast mode that is again responsible for the appearance of a Laplace operator (diffusion in imaginary time) in the Schroedinger equation. Since diffusion takes place in imaginary time, this still leaves us with a reversible equation, yet in a very different form from Dirac. In the Dirac picture, the elementary degrees of freedom (ψ_i) always move at the speed of light, and the reason why the physical signal (group speed) travels slower than c, $v/c = p/\sqrt{m^2c^2 + p^2}$, is because the spinors mix during the "collision" step, via the mass matrix. Indeed, $v/c = p/\sqrt{m^2c^2 + p^2} \to 1$ in the ultra-relativistic limit $m \to 0$. This shows that the Dirac dynamics really is a first-order Boltzmann-like stream-collide process! The Schroedinger picture, on the other hand, is much more similar to Navier-Stokes, the wavefunction velocity being given by $u_a = -\nabla_a S/m$, $\Phi = Re^{iS/\hbar}$ being the non-relativistic wavefunction in eikonal form.

Thus, in both cases, the first-order irreversible Boltzmann and the reversible Dirac dynamics, a macroscopic Advection-Diffusion (AD) paradigm *emerges* from an underlying Stream-Collide (SC) microscopic dynamics. Advection differs from streaming in that the motion proceeds along the fluid velocity instead of the particle one (light-speed for Dirac), Diffusion differs from Collision, in that no second order derivatives are ever required to drive the system to equilibrium.

It is here mantained that the SC paradigm is more natural and efficient than the AD one for computational purposes, especially with parallel computing in mind. The reasons are not hard to glean: streaming proceeds along *straight lines* in configuration space, since, at variance with the fluid velocity, the microscopic velocities do not depend on space or time. This is a major simplification in dealing with strong non-equilibrium systems, where kinetic energy (streaming/advection) dominates the scene. On the other hand, within the Boltzmann and Dirac pictures, collisions are *local* in spacetime, at variance with diffusion, which requires non-local nearest-neighbor spatial connections. This is again a major simplification, especially for parallel computing. To be noted that this observation runs counter common intuition, according to which the most efficient representation is the one involving the least number of degrees of freedom. This is not necessarily true; it is indeed known that coarse-graining (the process of reducing the degrees of freedom) gives rise to less equations, but often more complicated ones to solve.

Based on the Boltzmann-Dirac analogy in Majorana form, these advantages were realized and turned into a concrete computational scheme, the Quantum lattice Boltzmann (QLB) which we describe in the next section.

3. Quantum Lattice Boltzmann

The Boltzmann equation is mathematically hard to solve, on account of two reasons; first it lives in a 6 dimensional phase-space plus time, $(\vec{x}, \vec{v}; t)$ and second, the collision operator is a complicated quadratic integral in velocity space. For this reason, several simplified models of the Boltzmann equation have been proposed since the mid 50's. A particularly successful model is based on the so-called relaxation approximation, whereby the collision operator is replaced by a single-relaxation time form, $C(f, f) = \omega\ (f^{eq} - f)$, ω being the relaxation frequency. Another powerful simplification consists of replacing velocity space to a handful of discrete speeds. For the last two decades, a specific instance of discrete velocity models in relaxation form, known as lattice Boltzmann equation (LBE) has proven exceedingly useful to handle a broad class of complex flows, ranging from full turbulence all the way down to biopolymer translocation in nanopores [4]. The discrete Boltzmann equation reads as follows

$$\partial_t f_i + v_i^a \nabla_a f_i = -\Omega_{ij}(f_j - f_j^{eq}) \tag{8}$$

where the latin index a runs over spatial dimensions. In the above $f_i(\vec{x}, t) = \int f(\vec{x}, \vec{v}; t)\delta(\vec{v} - \vec{v}_i)dv$ is the probability of finding a particle at position $\vec{x}$ and time t with discrete velocity $\vec{v}_i$. The discrete form of the Boltzmann equation makes the analogy with the Dirac equation even tighter, in that the discrete distribution function is most naturally paralleled to the Dirac spinor ψ_i.

The explicit identifications are as follows

$$f_i \leftrightarrow \psi_i \tag{9}$$

$$v_i^a \leftrightarrow S_{ij}^a \tag{10}$$

$$\Omega_{ij} \leftrightarrow M_{ij} \tag{11}$$

Having laid down the analogy in formal terms, several caveats need to be considered with due care.

The main point is that the discrete index in the Boltzmann distribution refers to the linear momentum, i.e. translational invariance, while the spinorial index in the Dirac equation labels an internal degree of freedom responding to rotational symmetry. In a nutshell, spinors are not vectors!

This reflects in a number of structural mismatches. First, in general the $(2s + 1)$ values of the spinor index, do not match the number of discrete speeds, usually a subset of the 3^D neighbors in a cubic cell in D spatial dimensions (typically 9 in $D = 2$ and 19 in $D = 3$. Second, while each Boltzmann population f_i moves with a well prescribed discrete velocity v_i^a, only one of the three streaming matrices can be diagonalized at a time. In

other words, it is always possible to choose one direction where spin and momentum are aligned (chiral representation), but no more than one at a time. This means that in $D > 1$, spinor components mix while streaming (spinning particles), while classical particles don't. Finally, since Ψ_i is complex, and the corresponding density is given by $\rho_i = |\psi_i|^2$, number conservation implies that the mass matrix M_{ij} be anti-symmetric, whereas the Boltzmann relaxation matrix is symmetric, as it depends only on the scalar product between v_i^a and v_j^a.

Remarkably, all of these difficulties can be circumvented by a suitable form of operator-splitting.

Let us consider the case of spin 1/2 particles, with only two discrete states, aligned with, say, the $\mp z$ direction, labeled by $i = 1, 2$ respectively. First, one starts from the Dirac-Majorana representation in which the S^z matrix is diagonal, with eigenvalues ∓ 1, (in natural units $c = 1$), hence isomorphic to a discrete Boltzmann Equation with two discrete speeds $v_i^z = \mp 1$. In this representation, the Majorana mass matrix is simply $M_{11} = M_{22} = 0$, $M_{12} = -M_{21} = \omega_c$.

The stream-collide along z proceeds as follows (time-step made unit for simplicity):

$$\psi_i(z_i, y, x; t+1) - \psi_i(z, y, x; t) = M_{ij} \frac{(\psi_j(z, y, x; t) + \psi_j(z_j, y, x; t+1))}{2} \tag{12}$$

where $z_i = z + v_i^z = z \mp 1$, $i = -1, 1$, is the lattice neighbor pointed by the discrete speed $v_i^z = \mp 1$. In explicit terms, and omitting the y, x dependency which is left silent at this level,

$$\psi_1(z-1; t+1) - \psi_1(z; t) = \frac{m}{2}(\psi_2(z; t) + \psi_2(z+1; t+1)) \tag{13}$$

$$\psi_2(z+1; t+1) - \psi_2(z; t) = -\frac{m}{2}(\psi_1(z; t) + \psi_1(z-1; t+1)) \tag{14}$$

The lhs corresponds to an *exact* integration of the streaming operator along the characteristics $dz = \pm cdt$ (light-cones), which is typical of the Lattice Boltzmann method. The collision term at the rhs is integrated according to the trapezoidal (Crank-Nicolson) rule, in order to preserve the unitarity of the numerical scheme. the above 2×2 system can be readily inverted to deliver the quantum lattice Boltzmann scheme (QLB) is explicit form as

$$\psi_1(z-1; t+1) - \psi_1(z; t) = a\psi_1(z; t) + b\psi_2(z, ; t)) \tag{15}$$

$$\psi_2(z+1; t+1) - \psi_2(z; t) = -b(\psi_1(z; t) + a\psi_2(z; t)) \tag{16}$$

with matrix elements

$$a = \frac{1 - m^2/4}{1 + m^2/4} \tag{17}$$

$$b = \frac{m}{1 + m^2/4} \tag{18}$$

where $m \equiv \omega_c \Delta t$, is the dimensionless Compton frequency in lattice units ($\Delta t = 1$). It is readily shown that the above discrete system is unitary for any value of the time-step

Δt. This is the quantum lattice Boltzmamn (QLB) in one spatial dimension. It looks like a perfectly classical motion of two discrete walkers, hopping by one lattice unit along $\pm z$ at each time-step and colliding according to the scattering matrix given by the rhs. Next comes the stream-collide step along the next direction, say y. Here, a plain classical stream-collide does not work because the streaming matrix S^y is -not- diagonal. However, it is always possible to find a transformation matrix, say Y, such that $\tilde{S}^y = Y^{-1}S^yY$ is indeed diagonal, with eigenvalues ∓ 1. By introducing a transformed spinor $\psi^y = Y^{-1}\psi$ (indices relaxed for simplicity) and applying the matrix Y^{-1} to the Dirac equation, one can replicate the one-dimensional stream-collide algorithm along y, i.e. from $(z \mp 1, y, x)$ to $(z \mp 1, y \mp 1, x)$, only with a transformed mass matrix $\tilde{M}^y = Y^{-1}MY$. Once this stream-collide is performed, the original spinor is restored through $\psi = Y\psi^y$, where ψ^y is now the spinor *after* propagation along z and y. The same procedure can then be applied along the third and last direction, x, by means of the corresponding diagonalizing matrix X. Symbolically, the 3d evolution of the Dirac spinor reads like a sequence of three one-dimensional stream-collide steps:

$$\psi_i(z, y, x; t+1) = (X^{-1}P^xX)(Y^{-1}P^yY)P^z\ \psi_i(z \pm 1, y \pm 1, x \pm 1; t) \tag{19}$$

where $P^a = e^{(-S^a+M^a)}$ is the propagator along the direction a.

Of course, the operator splitting is not exact, as the streaming and collision matrices do not commute. However, the error is within the second order accuracy of the QLB scheme, and, most importanly, it does not spoil the unitarity of the scheme for any value of the timestep. Full details of the algorithm can be found in [5].

Here we only wish to offer a few general remarks. By starting from the Majorana representation of the Dirac equation, and resorting to an appropriate form of operator-splitting, the Dirac equation can be solved in terms of a time-explicit sequence of *classical* lattice trajectories and local collisions, supplemented with a rotation step. This offers significant computational advantages, especially on parallel computers, as we shall detail shortly.

4. Applications

The QLB has been applied to a variety of quantum wave problems. In the following, we present two selected applications for a relativistic and non-relativistic quantum problem, respectively. In the first example, the phenomenon of Anderson localization in expanding Bose-Einstein condensates (BEC), is investigated by numerically solving the Gross-Pitaevskii equation (GPE) with a random speckle potential [6]. In the second example, Klein tunneling in random media is studied, by simulating the propagation of a relativistic Gaussian wavepacket through a graphene sample with randomly distributed potential barriers [7].

4.1 Anderson localization in Bose-Einstein condensates

It is well known that disorder can profoundly affect the behavior of quantum systems, Anderson localization being one of the most fascinating phenomena in point [8]. Back in 1958, Anderson showed that the eigenstates of single quantum particles in a weak random potential can become localized, which means that the corresponding wave functions exhibit an exponential decay at large distances [9]. A large number of experimental and numerical studies have been devoted to the localization properties of Bose gases [9-17]. In particular, in [18], a theoretical and numerical study prescribes the conditions under which a one-dimensional BEC can exhibit Anderson localization. These conditions basically amount to require that the amplitude of the random potential be sufficiently large to promote destructive interference between free-propagating plane waves, and yet significantly smaller than the condensate energy, so as to avoid disruptive fragmentation of the wave function. In addition, the correlation length of the random potential should be smaller than the healing length of the condensate (the scale below which kinetic energy is dominant), so that noise can couple to a sizeable fraction of the spectrum of kinetic-energy carriers. In [6], we further investigated these conditions by means of a quantum lattice Boltzmann model (QLB) and we inspected the mechanism by which the localized state of the BEC is modified by the residual self-interaction in the (very) long-time term evolution of the condensate.

In practice, we studied the behavior of an expanding BEC in the presence of disorder in order to understand the interplay between non-linear interactions and disorder. The strength of the interaction is characterized by the inverse ratio of the initial healing length $\xi_h = \hbar/\sqrt{4m\mu}$, to the Thomas-Fermi length $L_{TF} = \sqrt{2\mu/m\omega_z^2}$, where μ is the chemical potential, m the boson mass and ω_z the longitudinal frequency of the optical trap [9]. The properties of random potential are summarized by its intensity V_R and correlation length σ_R. As shown in [18], for $\sigma_R < \xi_h$ and for a weak disorder $V_R/\mu < 1$, a one-dimensional BEC can exhibit Anderson localization.
Following the model proposed in [18], we considered a one-dimensional Bose-Einstein condensate trapped in an harmonic potential in the presence of a random potential $V(z)$. The corresponding Gross-Pitaevskii equation reads as follows:

$$i\hbar\partial_t\psi(z,t) = \left(-\frac{\hbar^2}{2m}\partial_z^2 + \frac{1}{2}m\omega_z^2 z^2 + V(z) + NU_1|\psi(z,t)|^2 - \mu\right)\psi(z,t), \qquad (20)$$

where U_1 is the coupling constant and μ is the chemical potential. The random potential $V(z)$ is taken in the form of a one dimensional speckle potential [14, 19-21].

Initially, the BEC is assumed to be at equilibrium in the harmonic trap, then the harmonic trap is removed and the BEC starts to freely expand. At time $t \gg 1/\omega_z$, the random potential is switched on. Starting from this model, in [18] it is shown that for $\sigma_R < \xi_h$ and when the random potential fulfills the condition

$$V_R \ll \mu(\xi_h/\sigma_R)^{1/2}, \qquad (21)$$

the BEC wave function undergoes Anderson localization. In particular, the large-distance

asymptotic behavior of the wave function density $n(z)$ is given by

$$n(z) \propto |z|^{-3/2} \exp(-2\gamma(1/\xi_h)|z|), \tag{22}$$

where $\gamma(k) = 1/L(k)$ is the Lyapunov exponent and $L(k)$ is the localization length. In [18], an approximation to $\gamma(k)$ is computed and related to the correlation properties of the disorder. For the speckle potential used in our work, one has [18]

$$\gamma(k) \sim \gamma_0(k)(1 - |k|\sigma_R)\Theta(1 - |k|\sigma_R), \quad \gamma_0(k) = \frac{\pi m^2 V_R^2 \sigma_R}{2\hbar^4 k^2}. \tag{23}$$

The QLB scheme solves GPE in the limit of "small" potential interaction. Hence, large values for the coupling constant β_{QLB} violate the adiabatic assumption. This implies limitations to the ratio between L_{TF} and ξ_h, where $L_{TF} = \sqrt{2\mu/m\omega_z^2}$ is the Thomas-Fermi half length. In practice, QLB is constrained to $\lambda \equiv L_{TF}/\xi_h \sim 10$.

It should be noted that our set of parameters is representative of current BEC experiments, although with possibly a weaker non-linearity, i. e. narrower separation between the outer and inner length-scales, L_{TF} and ξ_h, respectively (see e.g. the experimental work in [22] where $\lambda \sim 114$).

However, a scale separation $\lambda \sim 10$ is nonetheless sufficient to yield clear evidence of Anderson localization.

In particular, for the present simulations, parameters are set as follows:

$$\omega_z = 5 \times 10^{-3}, \quad \beta_{QLB} = 2, \quad \widetilde{m} = 1/4,$$

This set-up delivers $\mu = 0.01943$, $L_{TF} = 78.85$ and $\xi_h = 7.17$. The domain length is set to $L = 32000 \sim 400 L_{TF}$ and the simulation span at $T = 150/\omega_z = 30000$.
As a result, $\lambda = 10.997$ and we set $V_R = 0.2\mu$ and $\sigma_R = 0.5\xi_h$, so that $\sigma_R < \xi_h$ and condition of Eq. (21) are fulfilled. The wave function density is computed by averaging over the solutions obtained with 100 realizations of the speckle potential.

In Fig. 1, the averaged wave-function densities, computed at two different resolutions ($N_g = 32000$ and 128000 nodal points) by QLB are compared with numerical solutions obtained (at the same spatial resolution) by the standard Crank-Nicolson scheme as well as with the predicted asymptotic behavior given by Eq. (22). A very good agreement is observed.

In Ref. [18], it is argued that the expanding and then localized BEC might be a long-lived metastable state rather than a true ground-state solution. If so, the residual self-interaction should cause a long-term depletion of the BEC. The question arises as to whether such long-term depletion really occurs, and, if so, on which time-scale. In order to explore this question, we performed very-long time simulations up to time $t = 15000/\omega_z$, one hundred times longer than in the previous literature.

The averaged wave function densities at times $t = 1500/\omega_z$ and $t = 15000/\omega_z$ are compared with the one obtained at time $t = 150/\omega_z$, as shown in Fig. 2. The BEC is still well localized, but clearly on the way of loosing its localization. In particular, by fitting the

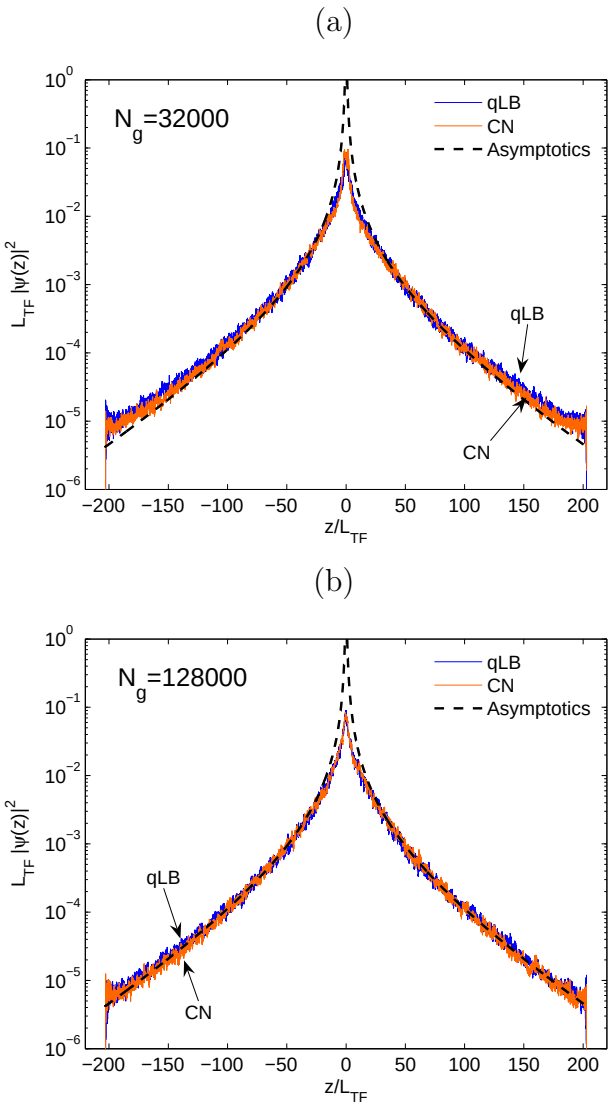

Figure 1 (Color online) Comparison between the averaged wave function densities computed by QLB and CN at two different resolutions. The numerical results are compared with the long-tail asymptotic behavior described by Eq. (22). Parameters are set as follows: $\omega_z = 5 \times 10^{-3}$, $\beta_{QLB} = 2$, $\widetilde{m} = 1/4$, $V_R = 0.2\mu$, $\sigma_R = 0.5\xi_h$, $\lambda = 10.997$, $T = 150/\omega_z$. (a) $N_g = 32000$, (b) $N_g = 128000$.

numerical wave function densities with the analytical curve $n(z) \propto |z|^{-3/2} \exp(-2\gamma|z|)$, the following time-decay law for γ is found (see Fig. 3):

$$L_{TF}\gamma(t) = \frac{0.055}{(\omega_z t)^{1/3}}. \tag{24}$$

In Fig. 2, the analytical curves obtained with the values of γ given by Eq. (24) for $t\omega_z = 150, 1500$ and 15000 are also shown. In Fig. 3, numerical results for $L_{TF}\gamma$ as a function of $\omega_z t$ are reported and compared with the scaling law, Eq. (24). For this numerical test, we used the QLB scheme with $N_g = 32000$ nodal points, while other parameters are set as before. Although a direct comparison with experimental results reported in [22] is not possible, since we are simulating a BEC with a weaker non-linearity ($\lambda \sim 11$ instead of $\lambda \sim 114$) and with a different value for the ratio σ_R/ξ_h, in Fig. 3 we report the

experimental value obtained in [22] for $\lambda = 114$, $\sigma_R/\xi_h \sim 0.7$ and $V_R/\mu = 0.2$. This last parameter is the same as in our simulations. The experimental result corresponds to a localization length of about $L_{loc} = 0.5$ mm, while in our simulation, we obtain $L_{loc} = 1.19$ mm.

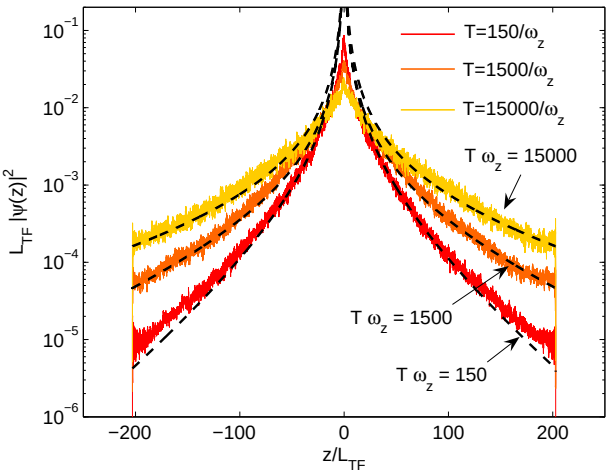

Figure 2 (Color online) Averaged wave function densities computed by QLB with $N = 32000$ discretization points up to times $T = 150/\omega_z$, $T = 1500/\omega_z$ and $T = 15000/\omega_z$. Parameters are set as follows: $\omega_z = 5 \times 10^{-3}$, $\beta_{QLB} = 2$, $\widetilde{m} = 1/4$, $V_R = 0.2\mu$, $\sigma_R = 0.5\xi_h$, $\lambda = 10.997$.

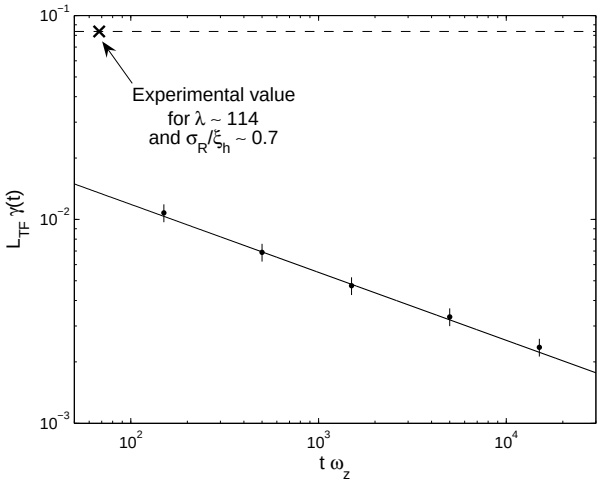

Figure 3 Numerical values of $L_{TF}\gamma$ at different times compared with the decaying law of Eq. (24). Parameters are set as follows: $\omega_z = 5 \times 10^{-3}$, $\beta_{QLB} = 2$, $\widetilde{m} = 1/4$, $V_R = 0.2\mu$, $\sigma_R = 0.5\xi_h$, $\lambda = 10.997$. Error bars indicate the min-max values over the ensemble of realizations. The $'X'$ point indicates the experimental result obtained in [22] for $V_R/\mu = 0.2$, as in our simulation, but for a different setting of λ and σ_R/ξ_h, which take the values 114 and 0.7, respectively.

The pictures show a clear delocalization trend in the very-long term evolution of the condensate, thereby supporting the conjecture that Anderson localization is a long-lived *metastable* state of the expanding condensate.

4.2 Relativistic electron transport in graphene

As opposed to classical quantum mechanics, where electrons tunneling into a barrier are exponentially damped, relativistic scattering was shown by Klein in 1929 [23] to follow a very unexpected behavior: If the potential is of the order of the electron mass or higher the barrier becomes virtually transparent to the electrons. This is called the Klein paradox. Experimental realizations were not available until the recent discovery of graphene [24, 25]. This material has revealed a series of amazing properties, such as ultra-high electrical conductivity, ultra-low shear viscosity to entropy ratio, as well as exceptional structural strength, as combined with mechanical flexibility and optical transparency. Moreover, due to the special symmetries of the honeycomb lattice, electrons in graphene are shown to behave like an effective Dirac fluid of *massless* chiral quasi-particles, propagating at a Fermi speed of about $v_F \sim c/300 \sim 10^6$ m/s.

Due to the fact that, under suitable conditions [26], electronic excitations in graphene behave as an effective relativistic Dirac fluid, in the presence of a random media, transport laws similar to the ones ruling fluid motion in diluted porous media, may be expected to apply. We refer here, e.g. to the Carman-Kozeny law [27, 28], which relates the permeability of a porous medium (conductivity of a graphene sample) to the solid concentration (impurity density).

In [7], we presented QLB numerical solutions of the Dirac equation in the presence of random impurities, thereby providing an estimate for the effects of the impurity concentration on the conductivity of the graphene sample, for both cases, massless and massive Dirac fermions.

One of the major technological challenges in current graphene research is to manufacture larger samples, above 10 microns, for practical use in engineering devices [29]. As the sample size is increased, however, it becomes more and more difficult to secure the purity of the sample, i.e. avoid crystalline inclusions (impurities) which alter the local structure of the graphene honeycomb lattice. Such impurities are indeed known to significantly affect the macroscopic properties of the sample, primarily its electrical conductivity. To gain insight into this problem, it is therefore of interest to investigate the propagation of relativistic wavepackets within a disordered sample. To analyze these transport phenomena, we simulate the propagation of a relativistic Gaussian wavepacket through a two-dimensional domain composed of three regions: an inlet region, where the wave packet is positioned at the initial time $t = 0$; the impurity region, i.e. the central part of the domain where randomly distributed barriers (impurities) are located; and the outlet region, which is the final region, where measurements of the transmitted wave packet are taken.

The impurity concentration is given by $C = Nd^2/A$, where N is the number of square obstacles of cross section d^2, distributed over an area $A = L_y \times L_z$. For the present simulations $d = 8$ (larger than the typical lattice distance of graphene) and C is varied in the range $0.001 \div 0.05$.

The lattice spacing is chosen in such a way as to properly resolve the smallest lengths

in the problem, namely the obstacle diameter D, as well as the wavepacket extent λ. The cell size is chosen to be $\Delta x = 0.96$nm, corresponding to $\sigma = 48$ lattice spacings for the spreading of the initial Gaussian wave packet, and $d = 8$ for the obstacle side. This yields a Fermi energy $E_F = 0.117$ (80meV in physical units).

In our study, we use two values for the mass of the particles, $m = 0$ for ungaped graphene and $m = 0.1$ ($mc^2 = 0.1\hbar/\Delta t \sim 0.07eV$ in physical units) for gaped graphene, and vary the impurity potential and the concentration. Five barrier heights are considered, namely $V = 25, 50, 100, 200, 285$ meV. Note that, while the first two lie below E_F, hence can be overcome classically, the others can only be traversed head-on via quantum tunnelling. It should be further observed, though, that since the wavepacket is wider than the single impurity, i.e. $\sigma > d$, even in the case $E_F < V$, the wavepacket can split and turn around the obstacle like a "classical" fluid. Our results can be classified according to the energy of the particles, the potential of the barrier, and their mass as follows: weak potentials, $V < E_F - mv_F^2$; intermediate potentials, $E_F - mv_F^2 < V < E_F + mv_F^2$; and strong potentials, $V > E + mv_F^2$. The transmission coefficient $T(t)$ is obtained by computing $T(t) = \int_{z>z_{out}} \rho(z, y, t) dz dy$, where ρ is the wave packet density defined as $\rho = |u_1|^2 + |u_2|^2 + |d_1|^2 + |d_2|^2$, with $\psi = (u_1, u_2, d_1, d_2)^T$ being the Dirac quadrispinor.

In order to provide a measurement of momentum dissipation, i.e. the loss of conductivity due to impurities, we compute the momentum transmission coefficient as follows:

$$T_{Jz}(t) = \int_{z>z_{out}} J_z(z, y, t) \quad dzdy, \tag{25}$$

where

$$J_z = \boldsymbol{\psi}^\dagger A_z \boldsymbol{\psi} + \boldsymbol{\psi}^\dagger A_z^\dagger \boldsymbol{\psi}, \tag{26}$$

is the z-component of the current density with A_z the streaming matrix along z and $\boldsymbol{\psi} = (u_1, u_2, d_1, d_2)^T$ the Dirac quadrispinor. In Fig. 4, we show some representative snapshots of the first 1800 time steps of the simulation, for impurity percentage $C = 0.5\%$ and $V = 50$ meV and for $m = 0$. Here, we can see the way how the wave packet is scattered by the impurities, generating a plane front, as a result of the fragmentation of the wavefunction due to the random obstacles.

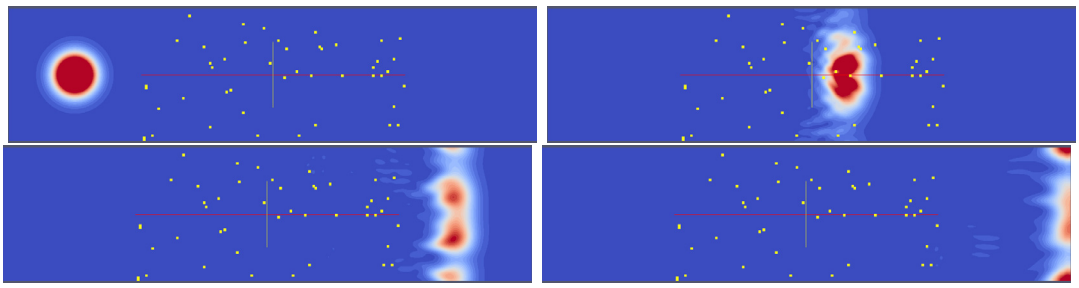

Figure 4 Wave packet density ρ at times = 0, 900, 1500, and 1800 (lattice units) for the simulation performed with impurity percentage $C = 0.5\%$ and $V = 50$ meV with $m = 0$.

As a quantitative result, we inspect the maximum of the transmission coefficient T_{Jz} as a function of the impurity potential and concentration, for three different values of

mass, $m = 0, 0.05, 0.1$ (see Fig. 5). These data summarize the loss of momentum, hence resistivity, due to the random impurities, formally measured by

$$\eta(C, V) = \max(T_{J_z}(C, V)) \quad . \tag{27}$$

From these figures, we observe that at high impurity concentration, $C = 0.05$, and a barrier $V = 100$ meV, the relativistic wavepacket looses about 50% of its momentum, as compared the case of a pure sample ($C = 0$). At the same concentration, a massive wave packet with $m = 0.1$, would loose more than 80%, indicating a significant drop of transmissivity due to inertia. At low impurity level, $C = 0.001$, both massless and massive wave-packets show a mild reduction of transmittivity, below 10%.

Let us now define the following "transmittance":

$$\Sigma(C, V) \equiv \frac{\eta}{1 - \eta} \quad . \tag{28}$$

This definition allows to draw a quantitative parallel with the concept of permeability of a classical fluid moving through a porous medium. That is, when the transmittance is unity, the conductivity goes formally to infinity, whereas zero transmittance connotes zero conductivity. Using Eqs. (27) and (28), we have found that the numerical results are satisfactorily fitted by the following analytical expression:

$$\Sigma(C, V) = A\frac{(1 - C)^{n+1}}{C^n} + \Sigma_0 \quad , \tag{29}$$

where A, n, Σ_0 are fitting parameters, which depend on the strength of the potential and the mass of the particles. In Fig. 5, we report the results of the fitting (solid line), showing good agreement with the numerical data. We have plotted η instead of Σ, in order to avoid the divergence at $C = 0$. The values of the parameters can be found in the original work, [7].

5. QLB for quantum computing and quantum field theory

Due to the one-sided nature of the space-time discretization, the light-cone streaming, as well as its low communication to computation ratio, QLB makes an excellent candidate for massively parallel implementations on current (electronic) computers. Even more exciting prospects, perhaps, open up in connection with *quantum* computing applications. Indeed, any complex wavefunction $q(\vec{x}; t) = c_u u(\vec{x}; t) + c_d d(\vec{x}; t)$, c_u and c_d being complex amplitudes, provides a natural representation of a q-bit, as a linear superposition of two upward and downward propagating quantum eigenstates, $u \equiv \psi_1$ and $d \equiv \psi_2$, respectively. As noted in [30], the stream-and-collide structure of the quantum lattice Boltzmann equation maps naturally onto the structure of quantum networks, i.e., quantum computing devices consisting of arrays of quantum logic gates, whose computational operation proceeds synchronously in time. The output of some gates is wire-connected to the input of some others (the streaming step), and locally processed by unitary operations (the collision step).

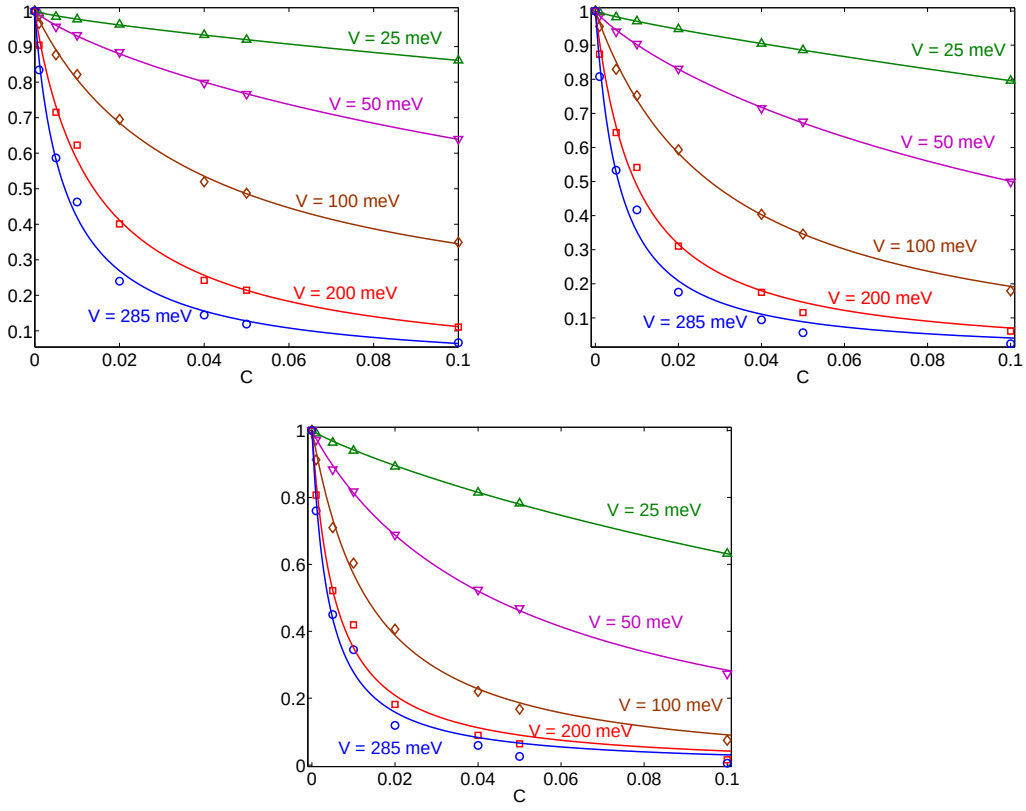

Figure 5 Maximum value of T_{Jz} as a function of the impurity percentage for each value of the impurity potential $V = 50 \div 285$. For three values of the mass, $m = 0$ (top), 0.05 (middle), 0.1 (bottom).

In compact notation:

$$\hat{\psi}_i = \psi'_i \tag{30}$$

where

$$\psi'_i(z, y, x; t) = \mathcal{C}_{ij}\ \psi_j(z, y, x; t) \tag{31}$$

is the post-collisional spinor associated with the collision matrix $\mathcal{C} \equiv \frac{1-M/2}{1+M/2}$, while

$$\hat{\psi}_i \equiv \mathcal{S}_i \psi_i = \psi_i(\vec{x} + \vec{v}_i; t + 1) \tag{32}$$

is the lightcone-shifted spinor, along the i-th lattice link.

QLB simulations of classical systems, emulating quantum computer operation, have indeed be performed in the recent past [31].

An important question is whether the QLB stream-collide unitary paradigm carries over from quantum mechanics to quantum field theory (QFT). Essentially, the idea is simply to apply the QLB scheme (13) to spinorial operators $\Psi_i(\vec{x}; t)$, instead of spinorial wavefunctions $\psi_i(\vec{x}; t)$. The point is to preserve the internal symmetries of such operators, a set of infinite-dimensional matrices in Hilbert space, under the stream-collide procedure.

This question has been answered in the affirmative in [32], where it was shown that, at least in $(1+1)$ dimensions, the QLB scheme is such to preserve the correct structure of

both bosonic and fermionic equal-time-commutators, thereby opening up potentially new perspectives for the simulation of quantum field theories in $(1+1)$ space-time dimensions.

As an example, it would be of interest to explore the possibility of realizing cold-atom QLB simulators for quantum field theory, along the lines developed for Hubbard-like lattice hamiltonians used in the simulation of interacting relativistic quantum field theories [33]. Tight analogies between the quantum-field-theory QLB scheme and such QFT lattice hamiltonians, although easily anticipated on a conceptual basis, remain quantitatively unexplored at the time of this writing. This makes an exciting topic for future research in the field.

6. Summary and outlook

Summarizing, we have discussed formal and substantial analogies between the Boltzmann equation of classical statistical physics and the Dirac equation for relativistic quantum wavefunctions. The special role of the Majorana representation of the Dirac equation, in which all matrices are real, in formulating a new class of computational schemes (Quantum Lattice Boltzmann method, QLB) for relativistic and relativistic quantum wave problems, has been emphasized. Selected applications of the QLB method, namely Anderson localization in Bose-Einstein condensates, and electronic transport in graphene, have been discussed and commented on. Finally, future prospects of QLB applications for quantum computing and the simulation of quantum field theories, have been briefly touched upon.

References

[1] E. Majorana, Il Nuovo Cimento, 5, 171, (1937).

[2] F. Wilczek, Nature, 5, 618, (2009).

[3] S. Succi, R. Benzi, Physica D, 69, 327, (1993).

[4] S. Succi, Europ. Phys. J B, 64, 471, (2008).

[5] S. Palpacelli, S. Succi, Comm. in Comp. Phys 4, 980, (2008).

[6] S. Palpacelli, S. Succi. Phys. Rev. E, 77, 066708 (2008).

[7] S. Palpacelli, M. Mendoza, H. J. Herrmann, S. Succi, *Klein Tunneling in the presence of random impurities*, (submitted).

[8] P. W. Anderson, Phys. Rev., 109, 1492 (1958).

[9] L. Sanchez-Palencia, Phys. Rev. A, 74, 053625 (2006).

[10] P. Lugan, D. Clément, P. Bouyer, A. Aspect, M. Lewenstein, L. Sanchez-Palencia, Phys. Rev. Lett., 98, 170403 (2007).

[11] C. Clément, A. F. Varón, M. Hugbart, J. A. Retter, P. Bouyer, L. Sanchez-Palencia, D. M. Gangardt, G. V. Shlyapnikov, A. Aspect, Phys. Rev. Lett., 95, 170409 (2005).

[12] C. Fort, L. Fallani, V. Guarrera, J. L. Lye, M. Modugno, D. S. Wiersma, M. Inguscio, Phys. Rev. Lett., 95, 170410 (2005).

[13] D. Clément, A. F. Varón, J. A. Retter, L. Sanchez-Palencia, A. Aspect, P. Bouyer, New J. Phys., 8, 165, (2006).

[14] M. Modugno, Phys. Rev. A, 73, 013606 (2006).

[15] E. Akkermans, S. Ghosh, Z. Musslimani, ArXiv Condensed Matter e-prints, cond-mat/0610579, (2006).

[16] T. Schulte, S. Drenkelforth, J. Kruse, W. Ertmer, J. Arlt, K. Sacha, J. Zakrzewski, M. Lewenstein, Phys. Rev. Lett., 95, 170411 (2005).

[17] J. E. Lye, L. Fallani, M. Modugno, D. S. Wiersma, C. Fort, M. Inguscio, Phys. Rev. Lett., 95, 070401 (2005).

[18] L. Sanchez-Palencia, D. Clément, P. Lugan, P. Bouyer, G. V. Shlyapnikov, A. Aspect, Phys. Rev. Lett., 98, 210401 (2007).

[19] , J. W. Goodman in *Laser Speckle and Related Phenomena*, Springer-Verlag, Berlin, edited by J. C. Dainty (1975).

[20] J. M. Huntley, Appl. Opt., 28, 4316 (1989).

[21] P. Horak, J. Y. Courtois, G. Grynberg, Phys. Rev. A, 58, 3953 (1998).

[22] J. Billy, V. Josse, Z. Zuo, A. Bernard, B. Hambrecht, P. Lugan, D. Clément, L. Sanchez-Palencia, P. Bouyer, A. Aspect, Nature, 453, 891 (2008).

[23] O. Klein, Zeitschrif Fr Physik a Hadrons and Nuclei, 53, 3-4, 157-165, (1929).

[24] K.S. Novoselov et al., Nature, 438, 197, (2005).

[25] K. Novoselov et al., Science, 306, 666, (2004).

[26] M. Muller, J. Schmalian and L. Fritz, Phys. Rev. Lett. 103, 025301, (2009).

[27] R.R. Rumer and P.A. Drinker, Proc. Am. Soc. Civil Eng., J. Hydraulic Div. 92 (HY5), pp. 155 (1966).

[28] J. Bear, Dynamics of Fluids in Porous Media, American Elsevier Publising Company (1972).

[29] Some references to technological applications can be found in A. H. Castro Neto, F. Guinea, N. M. R. Peres, K. S. Novoselov and A. K. Geim, Rev. Mod. Phys., 81, 1, 110 (2009).

[30] P. Love and B. Boghosian, Physica A, 362, 210 (2006).

[31] G. Vahala, J. Yepez and L. Vahala, Phys. Lett. A, 310, 187 (2003).

[32] S. Succi J. of Phys. A: Math. and Gen., 40, F559, (2007).

[33] J. I. Cirac et al, Phys. Rev. Lett., 105, 190403, (2010).